

2-27-2013

High-resolution dynamic atomic force microscopy in liquids with different feedback architectures

John Melcher
University of Bristol

David Martinez-Martin
Swiss Federal Institute of Technology, Zurich

Miriam Jaafar
Autonomous University of Madrid

Julio Gomez-Herrero
Autonomous University of Madrid

Arvind Raman
Birck Nanotechnology Center, Purdue University, raman@purdue.edu

Follow this and additional works at: <http://docs.lib.purdue.edu/nanopub>

 Part of the [Nanoscience and Nanotechnology Commons](#)

Melcher, John; Martinez-Martin, David; Jaafar, Miriam; Gomez-Herrero, Julio; and Raman, Arvind, "High-resolution dynamic atomic force microscopy in liquids with different feedback architectures" (2013). *Birck and NCN Publications*. Paper 1354.
<http://dx.doi.org/10.3762/bjnano.4.15>

This document has been made available through Purdue e-Pubs, a service of the Purdue University Libraries. Please contact epubs@purdue.edu for additional information.

High-resolution dynamic atomic force microscopy in liquids with different feedback architectures

John Melcher^{*1}, David Martínez-Martín², Miriam Jaafar³,
Julio Gómez-Herrero³ and Arvind Raman⁴

Full Research Paper

Open Access

Address:

¹Department of Engineering Mathematics, University of Bristol, Bristol BS8 1TR, United Kingdom, ²ETH Zürich, Department of Biosystems Science and Engineering, CH-4058 Basel, Switzerland, ³Departamento de Física de la Materia Condensada C-III, Universidad Autónoma de Madrid, 28049 Madrid, Spain and ⁴School of Mechanical Engineering and Birck Nanotechnology Center, Purdue University, West Lafayette, IN 47907

Email:

John Melcher^{*} - j.melcher@bris.ac.uk

^{*} Corresponding author

Keywords:

atomic force microscopy; dAFM; high-resolution; liquids

Beilstein J. Nanotechnol. **2013**, *4*, 153–163.

doi:10.3762/bjnano.4.15

Received: 03 December 2012

Accepted: 24 January 2013

Published: 27 February 2013

This article is part of the Thematic Series "Advanced atomic force microscopy techniques".

Guest Editors: T. Glatzel and U. D. Schwarz

© 2013 Melcher et al; licensee Beilstein-Institut.

License and terms: see end of document.

Abstract

The recent achievement of atomic resolution with dynamic atomic force microscopy (dAFM) [Fukuma et al., *Appl. Phys. Lett.* **2005**, *87*, 034101], where quality factors of the oscillating probe are inherently low, challenges some accepted beliefs concerning sensitivity and resolution in dAFM imaging modes. Through analysis and experiment we study the performance metrics for high-resolution imaging with dAFM in liquid media with amplitude modulation (AM), frequency modulation (FM) and drive-amplitude modulation (DAM) imaging modes. We find that while the quality factors of dAFM probes may deviate by several orders of magnitude between vacuum and liquid media, their sensitivity to tip-sample forces can be remarkable similar. Furthermore, the reduction in noncontact forces and quality factors in liquids diminishes the role of feedback control in achieving high-resolution images. The theoretical findings are supported by atomic-resolution images of mica in water acquired with AM, FM and DAM under similar operating conditions.

Introduction

Since its inception [1], dynamic atomic force microscopy (dAFM) has proven to be a powerful yet versatile tool capable of operating in media ranging from vacuum to liquids and interrogating samples ranging from stiff inorganic materials to soft biological samples, with nanoscale resolution. Recently, the achievement of atomic-resolution imaging in liquids [2-6] has

challenged the accepted belief that high quality factors, which are a hallmark of microcantilever probes in vacuum, are necessary for atomic-resolution imaging [7]. However, atomic-resolution images have now been obtained with several dAFM imaging modes in liquids despite the quality factors being several orders of magnitude smaller than in vacuum.

Several prior works have been dedicated to the understanding of imaging resolution and the role of feedback control in dAFM. Prior efforts to analyze imaging resolution in dAFM have typically focused on the small-amplitude limit in order to establish a relationship between various noise sources in the experimental setup and the minimum detectable gradient of the tip–sample force [1,4,8,9]. However, the optimal imaging amplitude in FM has also been considered [10]. The role of feedback control in dAFM and its stability have been studied largely by using numerical simulations to solve complex systems of nonlinear, integro-differential equations governing the deflection of the oscillating probe subject to feedback control [11–13]. Kilpatrick et al. [14] neglected tip–sample forces in order to provide an estimate for stable control parameters in FM. To improve imaging resolution in liquids, Q-controlled dAFM, which uses feedback control to manipulate the effective quality factor of the oscillating probe, has been proposed [15,16]. However, the merits of this approach for improving imaging resolution are still under question [17].

In this article we present a combined theoretical and experimental study of high-resolution imaging in liquid media with various dAFM imaging modes. The method of periodic averaging [18] is used to simplify the fast-time-scale equations governing the deflection of the oscillating probe by slow-time-scale, averaged equations that govern the amplitude and phase lag of the oscillation. The averaged equations provide a natural starting point for the analysis of closed-loop dAFM imaging modes, which are ultimately designed to regulate the amplitude and phase lag of the oscillating probe rather than its time-varying deflection. From the approximate theory, we explore performance metrics for dAFM imaging modes, such as (i) force sensitivity and resolution, (ii) detection bandwidth, (iii) disturbance mitigation and (iv) imaging stability. In support of our findings, we demonstrate atomic-resolution images of mica in water with FM, AM and DAM under similar operating conditions.

Analysis of closed-loop dAFM imaging modes

Conventional dAFM imaging modes use a microcantilever probe with a sharp tip affixed to the free-end, which is made to oscillate near its fundamental resonance in close proximity to a sample. Through the influence of tip–sample forces, the presence of the sample is detected in the oscillations of the probe. Let z denote the nominal separation between the tip and sample in the absence of tip–sample forces. The realization of a dAFM imaging mode follows from the implementation of a separation regulator that uses z as a controlled input for a feedback regulator designed to maintain the amplitude and/or phase lag of the oscillation. The actuation of z is implemented by a piezo actuator.

The values of z that satisfy the regulation objective are interpreted as the topography of the sample. The simplest dAFM imaging mode is AM, where the amplitude is maintained by the separation regulator, while the phase lag of the oscillation is free to vary. Imaging modes with more complex feedback architectures, such as FM and DAM, will be described later in this section.

In order to establish the performance metrics for high-resolution imaging, we start with the equation of motion describing the time-varying deflection $x(t)$ of the probe tip in the presence of tip–sample forces given by

$$\ddot{x} + \frac{\omega_0}{Q_0} \dot{x} + \omega_0^2 x = \frac{\omega_0^2}{k} \left[F \cos \omega t + F_{ts}(d, \dot{d}) \right], \quad (1)$$

where ω_0 , Q_0 and k are the unperturbed natural frequency, quality factor and stiffness of the probe, respectively, and F is the excitation force [19]. F_{ts} is the tip–sample interaction force, which depends explicitly on the tip–sample gap $d(t) = z + x(t)$ and its rate \dot{d} . In the absence of tip–sample forces with $\omega = \omega_0$ and $F = F_0$, the tip oscillates with an unconstrained amplitude $a_0 = F_0 Q_0 / k$. $F = F_0$ and $\omega = \omega_0$ are fixed in AM, but F and ω are adjusted by feedback regulators in FM and DAM.

The solution of Equation 1 can be separated into two parts, the first being the equilibrium deflection x^* in the absence of the excitation force, and, the second being oscillation about x^* . At each z , x^* is found by setting $\ddot{x} = \dot{x} = 0$ in Equation 1 and satisfies

$$kx^* = F_{ts}(z + x^*, 0). \quad (2)$$

The tip–sample forces are often characterized by an attractive ($\partial F_{ts} / \partial d > 0$), noncontact regime when d is sufficiently large, which gives way to a repulsive ($\partial F_{ts} / \partial d < 0$), contact regime as d is reduced. If $k < \partial F_{ts} / \partial d$, then for some z , x^* will be bistable. This results in one stable equilibrium for both the noncontact and contact regimes. In this case, a spontaneous transition from the noncontact equilibrium to the contact equilibrium, or *snap-in*, can occur [20]. The snap-in instability is avoided if the equilibrium deflection is monostable, which occurs when either z is sufficiently large for a given k or when k exceeds the maximum gradient of F_{ts} [10,21].

The model for the probe dynamics in Equation 1 can be simplified through the use of the method of first-order averaging [22,23]. To this end, consider the overall motion with excitation to be represented by $x(t) = x^* + a(t) \cos[\omega t - \phi(t)]$, where

$a(t)$ and $\phi(t)$ are the time-varying amplitude and phase lag, respectively [24]. An autonomous equation describing the dynamics of a and ϕ becomes:

$$\begin{aligned}\frac{da}{d\tau} &= \frac{F}{F_0} a_0 \sin \phi - a [1 + e_{ts}(z, a)], \\ \frac{d\phi}{d\tau} &= \frac{F}{F_0} \frac{a_0}{a} \cos \phi + \sigma + v_{ts}(z, a),\end{aligned}\quad (3)$$

where $\tau = \omega_0 t / 2Q$ and $\sigma = Q_0[(\omega/\omega_0)^2 - 1]$ is the frequency shift scaled by the half-power bandwidth of the resonance. The nonlinear tip-sample forces are captured in Equation 3 by the functionals

$$e_{ts}(z, a, x^*) = \frac{Q_0}{\pi k a} \int_0^{2\pi} F_{ts}(d(\theta), d'(\theta)) \sin \theta d\theta, \quad (4)$$

$$v_{ts}(z, a, x^*) = \frac{Q_0}{\pi k a} \int_0^{2\pi} F_{ts}(d(\theta), d'(\theta)) \cos \theta d\theta, \quad (5)$$

where $d(\theta) = z + x^* + a \cos \theta$ and $d'(\theta) = -a \sin \theta$. e_{ts} is the energy dissipated during the tip-sample interaction and v_{ts} is the virial of the tip-sample interaction [25]. The virial is related to the kinetic energy stored in the oscillating probe through the virial theorem [26] and is a measure of the maximum potential energy stored in the tip-sample interaction during an oscillation. Moreover, by introducing a specific model for F_{ts} , a relationship between v_{ts} and the interaction potential can be established [27]. Finally, both e_{ts} and v_{ts} have been nondimensionalized by the energy dissipated by the media during an oscillation cycle $E_{med} = \pi k a^2 / Q_0$. In one form or another, these parameters are ubiquitous in perturbation analysis of dAFM [22,23,26–28].

Equation 3 captures the transient response $a(\tau)$ and $\phi(\tau)$ of the oscillating probe. In addition to providing an approximate relationship between the experimental observables and the tip-sample forces, this feature accommodates the study of stability and detection bandwidth. The transient response of both the amplitude and phase lag have a nominal characteristic time scale of $2Q_0/\omega_0$ in the absence of tip-sample forces or feedback control. The equilibrium solutions a^* and ϕ^* of Equation 3 approximate steady-state, harmonic-oscillation solutions to Equation 1 with constant amplitude and phase lag, oscillating about the equilibrium deflection x^* . Note that we have included the dependence on x^* in Equation 4 and Equation 5 for completeness. However, unless the equilibrium deflection is bistable, i.e., near snap-in, x^* can be neglected in the analysis. This assumption is carried forward, and, in the subsequent analysis, we write $v_{ts}(z, a)$ and $e_{ts}(z, a)$.

Setting $da/d\tau = d\phi/d\tau = 0$ in Equation 3, we arrive at the equations governing the steady-state amplitude and phase lag

$$\begin{aligned}\frac{a^*}{a_0} &= \frac{F}{F_0} \left\{ \left[\sigma + v_{ts}(z, a^*) \right]^2 + \left[1 + e_{ts}(z, a^*) \right]^2 \right\}^{-\frac{1}{2}}, \\ \phi^* &= -\tan^{-1} \left(\frac{1 + e_{ts}(z, a^*)}{\sigma + v_{ts}(z, a^*)} \right),\end{aligned}\quad (6)$$

where the asterisk denotes the steady-state. The stability of the steady-state oscillation is determined by Equation 3.

The nonlinear terms v_{ts} and e_{ts} introduce the possibility of coexisting stable solutions to Equation 6, even when the equilibrium deflection is monostable [21,29,30]. When the equilibrium is bistable, three coexisting stable oscillation states are possible [31]. Such nonlinear phenomena are of considerable practical importance in dAFM and have been studied extensively in the literature [32–34].

Next, we introduce the feedback architectures that define the AM, FM and DAM imaging modes. AM is modeled with Equation 3 by setting $F = F_0$, $\sigma = 0$, and introducing a separation regulator that manipulates z :

$$z = -K_1 a - K_2 w; \quad \frac{dw}{d\tau} = a - a_{sp}, \quad (7)$$

where K_1 and K_2 are gain parameters. The control effort in Equation 7 consists of a proportional controller $K_1 a$ and an integral regulator $K_2 w$, which ensures $a^* = a_{sp}$. By substituting $F = F_0$, $\sigma = 0$ and $a^* = a_{sp}$ into Equation 6, it can be shown that the AM topography reflects a combination of the e_{ts} and v_{ts} and the resulting phase lag reveals the relative magnitude of the two. However, it is important that the issue of co-existing oscillation states persists in AM allowing the controller to spontaneously switch between stable states [30].

The FM and DAM imaging modes have more complex feedback architectures than AM. The original implementation of FM conceived by Albrecht et al. [8] used a self-excitation scheme where the excitation signal was generated by applying a phase shift to the deflection signal and the oscillation amplitude was maintained by a regulator. Alternatively, an externally generated, excitation signal and lock-in amplifier can be implemented to maintain a resonant excitation with constant oscillation amplitude [14]. The latter will be the focus of the present analysis. Both FM and DAM incorporate these auxiliary regulators that operate independently from the separation regulator:

$$\begin{aligned} F &= -K_1 a - K_2 w_1; \frac{dw_1}{d\tau} = a - a_{sp}, \\ \sigma &= -K_3 \phi - K_4 w_2; \frac{dw_2}{d\tau} = \phi - \phi_{sp}, \end{aligned} \quad (8)$$

where $K_1 - K_4$ are gain parameters, $a_{sp} = a_0$ and $\phi_{sp} = \pi/2$. The auxiliary regulators ensure that at steady-state, e_{ts} is captured in F and v_{ts} is captured in σ . While both the self-excited and externally excited implementations achieve the same objective, there are some differences in the detection bandwidth and measurement noise. These issues will be discussed briefly in the following section.

The auxiliary feedback regulators essentially have complete control over the oscillations of the probe through their independent manipulation of amplitude and phase lag. When equilibrium deflection x^* is monostable, coexisting of stable oscillation states, a^* and ϕ^* are eliminated by the integral regulators, while the stability and transient settling time can be controlled completely by the proportional controllers. It is straightforward to prove these results by substituting Equation 8 into Equation 3 and solving for the equilibrium points and the eigenvalues of the Jacobian matrix or by using standard tools for control theory [18]. Limitations in the control of the amplitude and phase lag are introduced only after incorporating the finite bandwidth of the amplitude and phase lag measurements into the model [14]. However, we note that instabilities persist when the equilibrium deflection x^* is bistable since the auxiliary regulators control the amplitude and phase lag but have no control over x^* .

The separation regulator in FM actuates z in order to maintain the frequency shift σ according to

$$z = -K_5 \sigma - K_6 w_3; \quad \frac{dw_3}{d\tau} = \sigma - \sigma_{sp}, \quad (9)$$

where K_5 and K_6 are gain constants, and σ_{sp} is the set-point frequency shift. At equilibrium in FM, the topography is purely a reflection of the virial of the interaction and the dissipation is measured in the corresponding excitation force signal.

The separation regulator in DAM actuates z in order to maintain the excitation force according to

$$z = -K_5 F - K_6 w_3; \quad \frac{dw_3}{d\tau} = F - F_{sp}, \quad (10)$$

where K_5 and K_6 are gain parameters and F_{sp} is the force at the set-point. At equilibrium in DAM, the topography is purely a reflection of the dissipation, and the virial is captured by the

corresponding frequency shift. In this respect, DAM can be regarded as the complementary mode to FM.

At this juncture, it is instructive to introduce some experimental data highlighting some of the key differences between dAFM operation in vacuum, air and liquid. In Figure 1, e_{ts} and v_{ts} are measured under typical operating conditions in vacuum, air and liquid with an oscillating probe that is controlled by the auxiliary feedback regulators in Equation 8 while z is displaced by a piezo actuator (see Methods for additional information). The coordinate z is shifted such that $z = 0$ is located approximately at the boundary between the contact and noncontact regimes. For high-resolution imaging, z is maintained in the neighborhood of $z = 0$. In vacuum, large long-range noncontact tip-sample forces result in $e_{ts} \gg 1$ and $|v_{ts}| \gg 1$ at imaging distances from the sample. Consequently, the oscillations of the probe are strongly influenced by the presence of tip-sample forces in vacuum. On the other hand, e_{ts} and v_{ts} are on the order of unity in air and small compared to unity in liquid.

Before proceeding, we will briefly address the issue of higher harmonics in liquids. Early work on dAFM in liquids showed

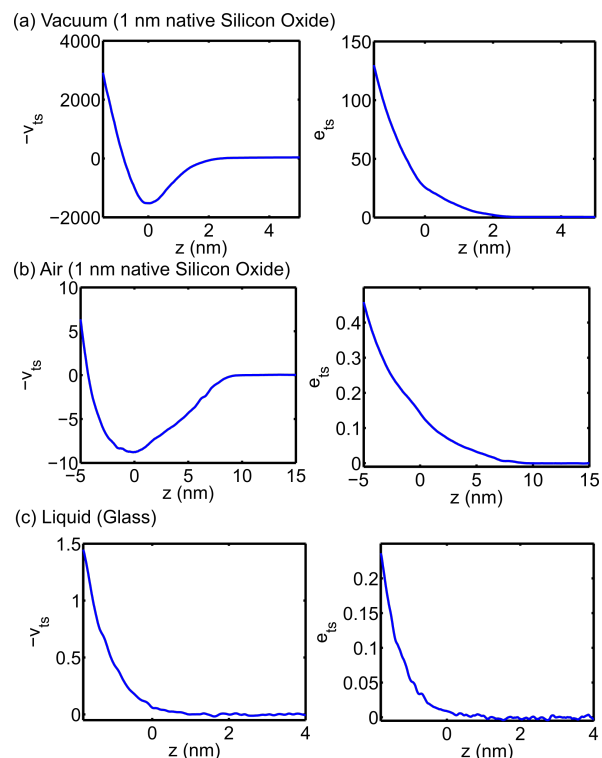


Figure 1: Experimental tip-sample virial $v_{ts}(z, a_{sp})$ and dissipation $e_{ts}(z, a_{sp})$. Data acquired in vacuum on a silicon sample with 1 nm native silicon oxide (a) in vacuum and (b) in air. (c) Data acquired in deionized water on a glass substrate. The set-point amplitudes were 8.5 nm, 8.6 nm, and 1.5 nm, respectively. See the Methods section for additional information.

that significant higher harmonic distortions in the oscillation waveform could provide additional channels for compositional mapping [35]. More recently, it was discovered that the use of soft microcantilevers (≤ 1 N/m) with quality factors close to unity resulted in higher harmonics from higher eigenmodes [36,37]. The present theory does not extend to soft microcantilevers in liquids. However, from prior work, we can expect that the primary difference for soft microcantilevers is that the dissipation reflects the energy lost to higher harmonics [38,39].

Performance metrics for high-resolution imaging in dAFM

Using the mathematical framework developed in the previous section based on the method of first-order averaging, we now address the question of high-resolution imaging in liquid, despite the low quality factors. We note that while the chemical makeup and atomic configuration of the tip and sample are important considerations for high-resolution imaging, the focus of this article is on the dAFM instrumentation. Specifically, we investigate the performance metrics for high-resolution imaging in dAFM, including (i) force sensitivity and resolution, (ii) detection bandwidth, (iii) disturbance mitigation and (iv) stability in dAFM modes.

Force sensitivity and resolution

To understand how atomic-resolution imaging is possible in liquids despite the low quality factors, we first examine the sensitivity of the oscillating probe to tip-sample forces. For high-resolution imaging in all dAFM imaging modes, the effect of small tip-sample forces between the foremost atom of the tip and the substrate must be detected in the steady-state amplitude and/or phase lag. Therefore, we are interested in the sensitivity of the steady-state amplitude and phase lag to a small perturbation to the total tip-sample force.

The tip-sample forces are limited in magnitude for a given length scale. These considerations are captured elegantly by an exponential function given by [10]

$$F_{ts}(d) = F_{ts0}e^{-d/\lambda}, d \geq 0, \quad (11)$$

where λ is the characteristic length scale and F_{ts0} is the magnitude corresponding to $d = 0$. The magnitude of F_{ts} is limited by requiring $d \geq 0$. Following [10], an approximate expression for the v_{ts} , which holds for an arbitrary amplitude, is given by

$$v_{ts}(z, a) = -\frac{Q_0 F_{ts0} e^{(a-z)/\lambda}}{k\lambda \left[1 + \sqrt{\frac{\pi}{2}} \left(\frac{a}{\lambda} \right)^{3/2} \right]}. \quad (12)$$

Choosing λ appropriately allows Equation 11 and Equation 12 to approximate a variety of tip-sample forces. Forces at the atomic scale are captured by $\lambda \approx 1$ Å.

The simple model for the tip-sample force in Equation 11 is conservative. Dissipative components of the interaction are more complex in nature and less understood. At the atomic scale, energy may be dissipated from the bulk motion of the tip due to spontaneous transitions between multistable configurations of the nearest atoms of the tip and sample [40,41]. To incorporate dissipation in a simplistic manner, we allow $e_{ts} = -\mu v_{ts}$, where μ is a proportionality constant. From the data in Figure 1, this appears to be a reasonable approximation when the force is unidirectional, which is the case for Equation 11.

Next, we perturb the steady-state amplitude and phase lag about their equilibrium by introducing a small variation in the tip-sample force. This is achieved by perturbing F_{ts0} by a small amount δF_{ts} . Using a first-order Taylor approximation of Equation 6 establishes a relationship between the amplitude and phase lag resolution, δa and $\delta \phi = \delta a/a$, respectively, and the force resolution, given by

$$\delta F_{ts}^{(a)} = S^{-1} \left[\frac{\left(\frac{|\sigma + v_{ts}|}{1 + e_{ts}} \right) + \mu}{\left(\frac{\sigma + v_{ts}}{1 + e_{ts}} \right)^2 + 1} \right]^{-1} \delta a, \quad (13)$$

$$\delta F_{ts}^{(\phi)} = S^{-1} \left[\frac{1 + \left(\frac{|\sigma + v_{ts}|}{1 + e_{ts}} \right) \mu}{\left(\frac{\sigma + v_{ts}}{1 + e_{ts}} \right)^2 + 1} \right]^{-1} \delta a, \quad (14)$$

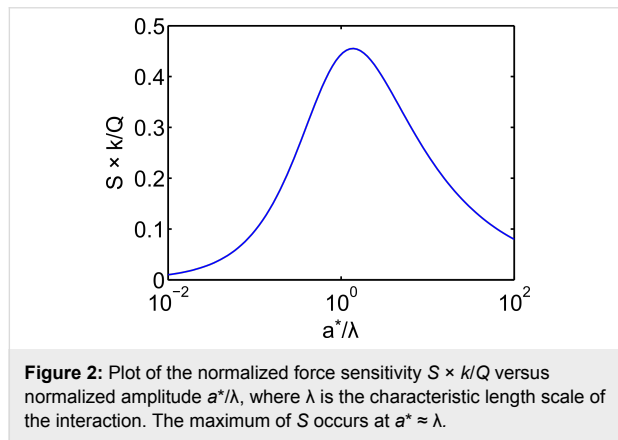
where

$$S = \frac{Q}{k} \frac{\left(\frac{a^*}{\lambda} \right)}{1 + \sqrt{\frac{\pi}{2}} \left(\frac{a^*}{\lambda} \right)^{3/2}}, \quad (15)$$

and $\delta F_{ts}^{(a)}$ and $\delta F_{ts}^{(\phi)}$ are the force resolutions in the amplitude and phase-lag measurements, respectively, and $Q = Q_0/(1 + e_{ts})$ is the effective quality factor.

Equation 13 and Equation 14 can be combined into a single approximation for force resolution in dAFM with the following approximation. Note that conventional dAFM modes are designed to excite the probe near its effective resonance frequency in the presence of the tip–sample forces. Thus, we argue that the term $(\sigma + \nu_{ts})/(1 + e_{ts})$ should be on the order of unity or smaller. It follows that the bracketed terms in Equation 13 and Equation 14 are on the order of unity allowing S to approximate the sensitivity of both the amplitude and phase-lag measurements to tip–sample forces. The force resolution can be approximated simply by $\delta F_{ts} = S^{-1} \delta a$.

Figure 2 plots the normalized force sensitivity $S \times k/Q$ versus the normalized amplitude a^*/λ . We note that much of the prior work of sensitivity and resolution in dAFM has linearized the tip–sample force to determine the minimum detectable force gradient [8]. Such analyses predict that force resolution in dAFM improves as the amplitude is increased. However, Equation 15, which holds for an arbitrary amplitude, predicts a global maximum in the force sensitivity for $a^* \approx \lambda$ (see Figure 2). This result is consistent with the analysis of FM by Giessibl et al. [10] but applies to all conventional dAFM modes.



To estimate the force resolution we must also obtain some estimate of the resolution of the amplitude measurement δa . Two important noise sources that contribute to δa are the thermal noise and deflection-sensor noise. In light of recent efforts to reduce the deflection-sensor noise [42], we will focus on the thermodynamic lower limit of δa , which can be approximated by [43]

$$\delta a^2 = \frac{2k_B T Q_0 B}{\pi k \omega_0}, \quad B < \frac{\pi \omega_0}{2Q_0} \quad (16)$$

where B is the measurement bandwidth, k_B is the Boltzmann constant and T is the temperature. Setting $B = \pi \omega_0 / 2Q_0$ extends the approximation in Equation 16 to large measurement band-

widths. However, the bandwidth restriction does not apply to self-excited FM [8,44]. Allowing $B \gg \omega_0/Q$ suggests that self-excited FM has the potential to be noisier than externally excited FM; however, this is a topic of ongoing debate [45,46].

Using Equation 16 to approximate δa yields to the following expression for δF_{ts} :

$$\delta F_{ts} = \frac{1 + \sqrt{\frac{\pi}{2} \left(\frac{a^*}{\lambda} \right)^2}}{\left(\frac{a^*}{\lambda} \right)} \sqrt{\frac{2k k_B T B}{\pi \omega_0 Q_0}}, \quad B < \frac{\pi \omega_0}{2Q_0}. \quad (17)$$

In the case of small amplitudes $a^* \ll \lambda$, substitution of

$$S \approx \frac{Q}{k} \left(\frac{a^*}{\lambda} \right)$$

and $\delta F_{ts} \approx \lambda \delta k_{ts}$ Equation 17, where k_{ts} is the tip–sample gradient, yields

$$\delta k_{ts} = \sqrt{\frac{2k k_B T B}{\pi \omega_0 Q_0 \left(a^* \right)^2}}, \quad a^* \ll \lambda, \quad (18)$$

which is essentially the result obtained by Albretch et al. [8]. However, of the two expressions, only Equation 17 captures the range of amplitudes applicable to high-resolution imaging.

The present analysis of the force sensitivity in dAFM begins to shed light on how high-resolution imaging is possible with dAFM in liquids despite the low quality factors. Table 1 lists the force sensitivity S and resolution δF_{ts} for several prior works demonstrating atomic resolution in vacuum and liquid environments. While Q_0 degrades by four orders of magnitude in liquid, the force resolution, in some cases, is of the same order of magnitude. Moreover, the force resolution approximated from Giessibl et al. [47] is in accordance with all the measurements in liquids. This result is the direct consequence of the small attractive forces in liquids on clean, hard surfaces, such as mica, that allow $a_{sp} \approx \lambda$ with a probe that is much softer than the tuning fork [2]. In vacuum, strong attractive forces cause the tip to snap into the surface when oscillation amplitudes are small.

From the data in Table 1, we must also entertain the possibility that force resolution is not necessarily the limiting factor for

Table 1: Parameters in atomic-resolution imaging in vacuum and liquid medium. S (Equation 15) and $\delta F_{ts} = S^{-1}\delta a$ (Equation 17) were calculated assuming $\lambda = 1$ Å, $T = 300$ K and $B = 1$ kHz, and $Q = Q_0$ and $a^* = a_{sp}$.

Mode	Med.	k (N/m)	a^* (nm)	Q_0	B_{osc} (Hz)	$\log_{10}S$	$\log_{10}\delta F_{ts}$	Ref.
FM	Vac.	17	34	28,000	2	1.9	−11.4	[49]
FM	Vac.	41	14.8	38,000	2	1.8	−11.6	[50]
AM	Vac.	60	0.2	550	15	0.61	−11.5	[51]
AM	Vac.	1600	0.28	18,000	50	0.58	−12.2	[52]
FM	Vac.	1800	0.8	4000 ^a	15	−0.22	−10.8	[47]
FM	Liq.	37	0.33	23	3000	−0.62	−10.7	[2]
PM ^b	Liq.	19	0.59	5.8	12,000	−1.0	−10.5	[3]
AM	Liq.	0.76	0.5	2 ^c	1300	−0.057	−10.3	[5]
FM	Liq.	30	0.59	8	8100	−1.1	−10.4	[4]
FM	Liq.	26	0.11	8.3	8400	−0.84	−10.6	[6]

^ataken from [48]. ^bphase modulation. ^ctaken from our own data.

imaging resolution. The highest resolution images are achieved with the qPlus sensor in [47], which has the lowest force resolution amongst the references in vacuum. If the force sensitivity meets some minimal requirements, the imaging resolution may be limited by other factors, such as the imaging stability [48]. Furthermore, the minimal requirement for force resolution may be less in liquids compared to vacuum where stable images can be acquired in the contact regime.

Detection bandwidth

The overall detection bandwidth in dAFM can be limited by the bandwidth of the amplitude and phase measurements, or the transient response, or the response of the oscillating probe. Drift in dAFM, for example arising from the piezo actuators controlling the image raster, imposes a minimum scan speed and corresponding detection bandwidth requirement for high-resolution imaging. Giessibl et al. [10] approximate the required detection bandwidth as 1 kHz. From our own experiments (see Methods section), we also estimate that the required bandwidth is on the order of 1 kHz for high-resolution imaging; however, we can expect variability depending on the experimental setup.

Detection of tip–sample forces in dAFM requires that the oscillating probe reaches a steady-state and the separation regulator achieves its objective. Thus, the detection bandwidth is limited by the transient settling time of the oscillating probe. As we have discussed, the amplitude and phase lag evolve on a characteristic time scale of $2Q_0/\omega_0$, which corresponds to the ring-down time of the probe in the absence of tip–sample forces and without feedback control. The corresponding bandwidth (rad/s) is

$$B_{osc} = \frac{\omega_0}{2Q_0}. \quad (19)$$

However, it is important to note that in the presence of tip–sample forces, the settling time can potentially be much longer. Such is the case when operating close to a bifurcation point between stable and unstable amplitude branches [21,31].

The feedback control plays an important role in determining the detection bandwidth in dAFM. As we have discussed, the auxiliary regulators in FM and DAM essentially have complete control over the oscillations of the probe, including the transient settling time. In [53], it was determined experimentally that FM and DAM can achieve similar detection bandwidths in vacuum. We remark that self-excited FM has a detection bandwidth of ω_0 [8], but only when operating in the linear regime ($a^* \ll \lambda$), which is rarely the case in high-resolution imaging. In a nonlinear regime, the frequency shift is coupled to the amplitude response [12], and the detection bandwidth is limited accordingly. Thus, the amplitude regulator in self-excited FM determines the overall detection bandwidth for high-resolution imaging when B_{osc} is small. On the other hand, the measurement bandwidth in AM is limited roughly by the oscillator bandwidth B_{osc} .

Table 1 lists B_{osc} for high-resolution images in vacuum and liquid. The two AM references in vacuum achieve a relatively high bandwidth in vacuum by using nonstandard probes. Kawai and Kawakatsu [52] exploited a higher eigenmode of a silicon cantilever that had an unperturbed resonance frequency of 1.8 MHz. Erlandsson et al. [51] used a tungsten wire with an unperturbed quality factor of just 550 in vacuum. The references for FM in vacuum in Table 1 rely on feedback control to improve the detection bandwidth by about one order of magnitude over standard probes, yet still fall far short of our 1 kHz estimation. On the other hand, the low Q 's in liquids ensure that the bandwidth requirement is met without including the auxil-

ary feedback regulators (again, see Table 1). Consequently, AM is more successful at high-resolution imaging in liquids than in vacuum.

Disturbance mitigation

A critical function of the feedback regulation in dAFM is to sustain the probe oscillations in the presence of unknown tip-sample forces, i.e., to mitigate disturbances from the tip-sample forces. In vacuum, the auxiliary regulators used in FM and DAM are essential for sustaining the oscillations in the presence of large noncontact tip-sample forces. Giessibl et al. [10] postulate that $e_{ts} < 1$ is required to maintain stable oscillations. However, the data in Figure 1 show that the auxiliary regulators are capable of maintaining stable oscillations when the magnitudes of e_{ts} and v_{ts} are much larger than unity. On the other hand, the approach taken in AM is simply to limit the magnitudes of e_{ts} and v_{ts} , in order to keep the amplitude from being attenuated. For example, choosing $a_{sp}/a_0 = 1/2$ in AM requires that the magnitudes of e_{ts} and v_{ts} do not exceed unity according to Equation 6. This limited approach to feedback regulation in AM can be problematic in vacuum and air where noncontact forces are large, but it is generally sufficient for imaging in liquids.

Stability

A final issue surrounding the high-resolution imaging in dAFM is stability. We have already discussed the importance of the auxiliary regulators in eliminating bistable oscillation states and maintaining stable oscillations in the presence of tip-sample forces. We turn now to the issue of global stability of the separation regulator. We first consider a stability issue that is inherent in FM, commonly referred to as “tip crash” [54]. To simplify matters, we require that z is manipulated slowly by the separation regulator such that the auxiliary feedback regulators maintain the probe oscillations in a quasi-steady state. Setting $K_5 = 0$ and requiring K_6 to be small in Equation 9, the dynamics of z in FM are approximated by

$$\frac{dz}{d\tau} = -K_6 \left[\sigma(z, a_{sp}) - \sigma_{sp} \right] \quad (20)$$

where $\sigma_{sp} = -v_{ts}(z, a_{sp})$.

The schematic in Figure 3 shows the typical behavior of $\sigma(z, a_{sp})$ in vacuum or air where attractive forces are significant. The arrows indicate the direction in which z is instructed to move by the feedback regulator according to Equation 20. The equilibrium points z^* are the zero crossings of $\sigma(z, a_{sp}) - \sigma_{sp}$. It is shown in Figure 3 that equilibrium in the attractive regime is locally stable but lacks global stability. A perturbation in the tip-sample forces can cause the separation regulator to ap-

proach the sample indefinitely. The closer σ_{sp} is to the onset of repulsive forces, the more likely is the onset of this instability. On the other hand, separation regulator in DAM is designed to maintain e_{ts} . When the amplitude is constant, e_{ts} typically increases monotonically with respect to z (see Figure 1); a point that was originally made in [55]. Consequently, DAM allows the oscillating probe tip to pass through the boundary between attractive and repulsive forces without necessarily resulting in a loss of stability.

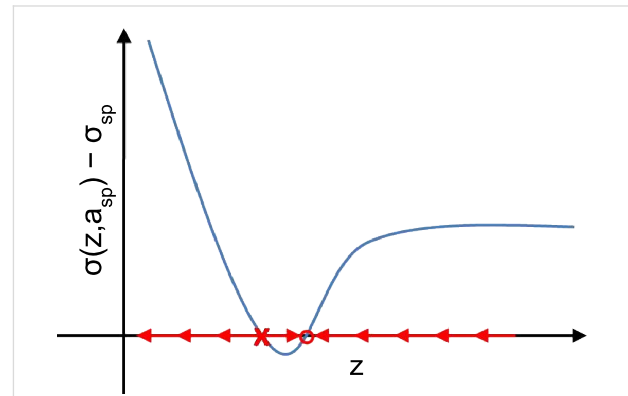


Figure 3: Stability of the z control in FM in vacuum. Arrows indicate the direction of the motion of z when placed under feedback control according to $dz/d\tau = -K_6[\sigma(z, a_{sp}) - \sigma_{sp}]$, where $K_6 > 0$.

Results and Discussion

In the previous sections, we investigated the role of the feedback control in high-resolution imaging. It is important to note that the task of regulating the oscillations of the probe under imaging conditions is greatly simplified in liquids due to the small long-range forces and low quality factors. Consequently, imaging modes with limited feedback control, such as AM, can be successful at high-resolution imaging in liquids [5]. In this section we present high-resolution images of mica in liquids with FM, DAM and AM acquired with the same probe and under similar operating conditions.

Figure 4 shows the topography and compositional images of freshly cleaved muscovite mica in water. Superimposed on the FM topography image is the theoretical structure of freshly cleaved muscovite mica, which exposes a plane of oxygen atoms (blue), which is slightly offset from a plane of silicon atoms (green) [2]. The FM dissipation image reveals a strong correlation with the FM topography image revealing dissipation on the atomic scale. The atomic-scale features in the FM dissipation image entertain the possibility of atomic-resolution imaging with DAM through regulation based on the tip-sample dissipation. This is indeed shown to be the case in Figure 4c. Similarly, atomic resolution is demonstrated in AM in Figure 4e. While topography images in AM reflect a combina-

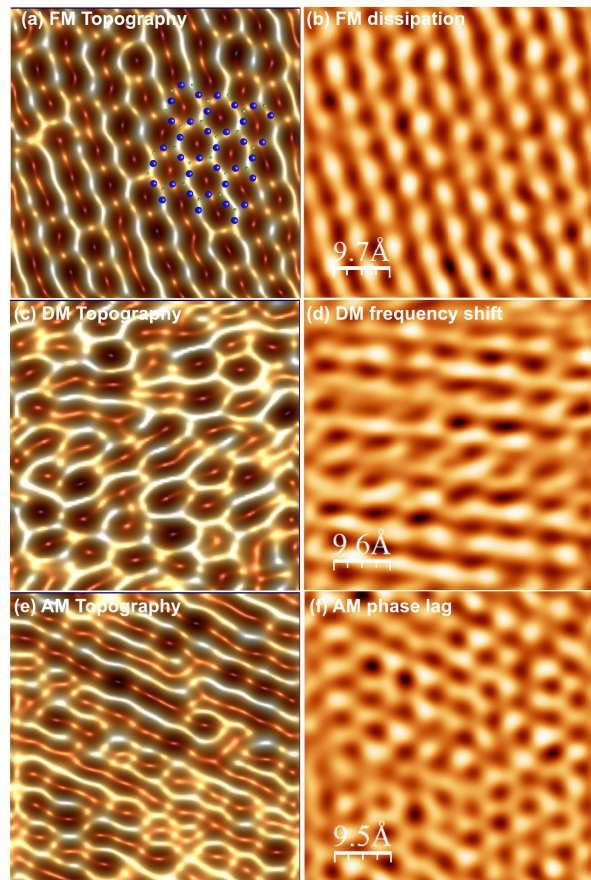


Figure 4: High-resolution images of mica in water taken with FM, DAM and AM. FM (a) topography and (b) dissipation. DAM (c) topography and (d) frequency-shift images. AM (e) topography and (f) phase-lag image. The variation in height in FM, DAM and AM topography images is 20, 80 and 40 pm, respectively, while the root-mean-squared surface roughness is 4, 13, and 6 pm, respectively. See Methods for additional specifications.

tion of the dissipation and virial, AM is more sensitive to the dissipation at high amplitude set-points, in which case AM resembles DAM.

The primary difference between the topography images in FM, DAM and AM in liquids is the treatment of tip-sample forces by the separation regulator. Of the three imaging modes, it appears that FM most faithfully reproduces the expected theoretical structure of freshly cleaved mica. From the data presented, it appears that regulation of the conservative component of the interaction captured by the virial is more favorable for atomic-resolution imaging. Furthermore, from Figure 1, we note that the magnitude of the virial is often larger than the dissipation for stiff inorganic samples such as mica. However, we stress that it was possible to obtain high-resolution images of mica in water in each of the three imaging modes under similar operating conditions.

Methods

The approach curves in Figure 1 were obtained by using the auxiliary regulators described in Equation 8, which is the typical precursory experiment to imaging with FM. The experimental data consist of F and σ versus z . Reconstruction of e_{ts} and v_{ts} versus z is achieved by substituting $a^* = a_0 = a_{sp}$ and $\phi^* = \pi/2$ into Equation 6 to yield

$$e_{ts}(z, a_{sp}) = a_{sp} \frac{F}{F_0} - 1, \quad (21)$$

$$v_{ts}(z, a_{sp}) = -\sigma. \quad (22)$$

Measurements were made on a silicon substrate with 1 nm native silicon oxide in vacuum with $k = 27$ N/m, $Q_0 = 28,000$ and $a_{sp} = 8.5$ nm and in ambient air with $k = 36$ N/m, $Q_0 = 620$ and $a_{sp} = 8.6$ nm. Data were acquired on glass in deionized water with $k = 0.6$ N/m, $Q_0 = 1.6$ and $a_{sp} = 1.5$ nm.

The high-resolution images of freshly cleaved mica in deionized water in Figure 4 were acquired with a Nanosensors™ PPP-NCH probe ($k = 40$ N/m, $Q_0 = 11$). Images were obtained in FM with $a_{sp} = 0.7$ nm, $\sigma_{sp} = 0.01$, in AM with $a_0 = 0.6$, $a_{sp} = 0.86a_0$, and in DAM with $a_{sp} = 0.4$ and $F_{sp} = 1.3F_0$. A wavelet filter with a scale of 0.13 nm was applied to each image by using the WSxM software [56]. The scan rate in the fast scan direction of the image raster is 440 nm/s, which was necessary to compensate for thermal drifts. For this scan rate, we calculate the required measurement bandwidth to be about 1 kHz for high-resolution imaging. All data were acquired with Nanotec Electrónica microscopes (Nanotec Electrónica S.L., Madrid, Spain) by using the WSxM software.

Conclusion

Through analysis and experiment, we have studied the performance metrics for high-resolution imaging in liquids with different dAFM imaging modes. In general, we find that while the quality factors of probes in liquids are typically low, the force sensitivity can be preserved by using soft probes with small amplitudes. Remarkably, it is possible for a probe in liquid to have a force sensitivity on par with the qPlus sensor in vacuum. Moreover, we find that the reduction in both attractive forces and quality factors that occurs in liquids decreases the importance of feedback control in obtaining stable, high-resolution images in liquids. Thus, the considerable advantages of FM over AM in obtaining high-resolution images in vacuum are not reproduced in liquids. These findings are supported by high-resolution images of mica obtained with FM, AM and DAM in liquid under similar operating conditions. From the data, it does

appear that FM still has some advantage over AM and DAM in atomic-resolution imaging. On the other hand, DAM offers robust stability for a range of environments and applications [53].

Acknowledgements

This research was supported by the National Science Foundation under Grant No. CMMI-0927648.

References

- Martin, Y.; Williams, C. C.; Wickramasinghe, H. K. *J. Appl. Phys.* **1987**, *61*, 4723–4729. doi:10.1063/1.338807
- Fukuma, T.; Kobayashi, K.; Matsushige, K.; Yamada, H. *Appl. Phys. Lett.* **2005**, *87*, 034101. doi:10.1063/1.1999856
- Fukuma, T.; Kilpatrick, J. I.; Jarvis, S. P. *Rev. Sci. Instrum.* **2006**, *77*, 123703. doi:10.1063/1.2405361
- Fukuma, T. *Jpn. J. Appl. Phys.* **2009**, *48*, 08JA01. doi:10.1143/JJAP.48.08JA01
- Voitchovsky, K.; Kuna, J. J.; Contera, S. A.; Tosatti, E.; Stellacci, F. *Nat. Nanotechnol.* **2010**, *5*, 401–405. doi:10.1038/nnano.2010.67
- Suzuki, K.; Oyabu, N.; Kobayashi, K.; Matsushige, K.; Yamada, H. *Appl. Phys. Express* **2011**, *4*, 125102. doi:10.1143/APEX.4.125102
- Giessibl, F. J.; Quate, C. F. *Phys. Today* **2007**, *60*, 17.
- Albrecht, T. R.; Grütter, P.; Horne, D.; Rugar, D. *J. Appl. Phys.* **1991**, *69*, 668–673. doi:10.1063/1.347347
- Wutscher, E.; Giessibl, F. J. *Rev. Sci. Instrum.* **2011**, *82*, 093703. doi:10.1063/1.3633950
- Giessibl, F. J.; Bielefeldt, H.; Hembacher, S.; Mannhart, J. *Appl. Surf. Sci.* **1999**, *140*, 352–357. doi:10.1016/S0169-4332(98)00553-4
- Nony, L.; Boisgard, R.; Aimé, J.-P. *Eur. Phys. J. B: Condens. Matter Complex Syst.* **2001**, *24*, 221–229. doi:10.1007/s100510170009
- Gauthier, M.; Pérez, R.; Arai, T.; Tomitori, M.; Tsukada, M. *Phys. Rev. Lett.* **2002**, *89*, 146104. doi:10.1103/PhysRevLett.89.146104
- Payton, O.; Champneys, A. R.; Homer, M. E.; Picco, L.; Miles, M. J. *Proc. R. Soc. A* **2010**, *467*, 1801–1822. doi:10.1098/rspa.2010.0451
- Kilpatrick, J. I.; Gannepalli, A.; Cleveland, J. P.; Jarvis, S. P. *Rev. Sci. Instrum.* **2009**, *80*, 023701. doi:10.1063/1.3073964
- Tamayo, J.; Humphris, A. D. L.; Owen, R. J.; Miles, M. J. *Biophys. J.* **2001**, *81*, 526–537. doi:10.1016/S0006-3495(01)75719-0
- Hölscher, H.; Schwarz, U. D. *Appl. Phys. Lett.* **2006**, *89*, 073117. doi:10.1063/1.2336723
- Ashby, P. D. *Appl. Phys. Lett.* **2007**, *91*, 254102. doi:10.1063/1.2824576
- Khalil, H. K. *Nonlinear Systems*; Prentice Hall: Upper Saddle River, NJ, 2002.
- Melcher, J.; Hu, S.; Raman, A. *Appl. Phys. Lett.* **2007**, *91*, 053101. doi:10.1063/1.2767173
- Butt, H.-J.; Cappella, B.; Kappl, M. *Surf. Sci. Rep.* **2005**, *59*, 1–152. doi:10.1016/j.surfrep.2005.08.003
- Lee, S. I.; Howell, S. W.; Raman, A.; Reifengerger, R. *Phys. Rev. B* **2002**, *66*, 115409. doi:10.1103/PhysRevB.66.115409
- Wang, L. *Appl. Phys. Lett.* **1998**, *73*, 3781–3783. doi:10.1063/1.122893
- Hu, S.; Raman, A. *Appl. Phys. Lett.* **2007**, *91*, 123106. doi:10.1063/1.2783226
- Eq. 3 is strictly valid for $Q \gg 1$ and $\omega \approx \omega_0$.
- The virial, as defined in Eq. 5, refers only to the oscillatory component of the force and includes a additional scaling of 2π for convenience.
- San Paulo, Á.; García, R. *Phys. Rev. B* **2001**, *64*, 193411. doi:10.1103/PhysRevB.64.193411
- Giessibl, F. J.; Bielefeldt, H. *Phys. Rev. B* **2000**, *61*, 9968–9971. doi:10.1103/PhysRevB.61.9968
- Anczykowski, B.; Gotsmann, B.; Fuchs, H.; Cleveland, J. P.; Elings, V. B. *Appl. Surf. Sci.* **1999**, *140*, 376–382. doi:10.1016/S0169-4332(98)00558-3
- Anczykowski, B.; Krüger, D.; Fuchs, H. *Phys. Rev. B* **1996**, *53*, 15485–15488. doi:10.1103/PhysRevB.53.15485
- García, R.; San Paulo, A. *Phys. Rev. B* **1999**, *60*, 4961–4967. doi:10.1103/PhysRevB.60.4961
- Rützel, S.; Lee, S. I.; Raman, A. *Proc. R. Soc. London, Ser. A* **2003**, *459*, 1925–1948. doi:10.1098/rspa.2002.1115
- García, R.; Pérez, R. *Surf. Sci. Rep.* **2002**, *47*, 197–301. doi:10.1016/S0167-5729(02)00077-8
- Raman, A.; Melcher, J.; Tung, R. *Nano Today* **2008**, *3*, 20–27. doi:10.1016/S1748-0132(08)70012-4
- Stark, R. W. *Mater. Today* **2010**, *13*, 24–32. doi:10.1016/S1369-7021(10)70162-0
- van Noort, S. J. T.; Willemsen, O. H.; van der Werf, K. O.; de Grooth, B. G.; Greve, J. *Langmuir* **1999**, *15*, 7101–7107. doi:10.1021/la990459a
- Basak, S.; Raman, A. *Appl. Phys. Lett.* **2007**, *91*, 064107. doi:10.1063/1.2760175
- Xu, X.; Melcher, J.; Basak, S.; Reifengerger, R.; Raman, A. *Phys. Rev. Lett.* **2008**, *102*, 060801. doi:10.1103/PhysRevLett.102.060801
- Melcher, J.; Carrasco, C.; Xu, X.; Carrascosa, J. L.; Gómez-Herrero, J.; de Pablo, P. J.; Raman, A. *Proc. Natl. Acad. Sci. U. S. A.* **2009**, *106*, 13655–13660. doi:10.1073/pnas.0902240106
- Martinez-Martin, D.; Carrasco, C.; Hernando-Perez, M.; de Pablo, P. J.; Gomez-Herrero, J.; Perez, R.; Mateu, M. G.; Carrascosa, J. L.; Kiracofe, D.; Melcher, J.; Raman, A. *PLoS One* **2012**, *7*, e30204. doi:10.1371/journal.pone.0030204
- Martínez, N. F.; Kamiński, W.; Gómez, C. J.; Albonetti, C.; Biscarini, F.; Pérez, R.; García, R. *Nanotechnology* **2009**, *20*, 434021. doi:10.1088/0957-4484/20/43/434021
- Kamiński, W.; Pérez, R. *Tribol. Lett.* **2010**, *39*, 295–309. doi:10.1007/s11249-010-9662-9
- Fukuma, T.; Kimura, M.; Kobayashi, K.; Matsushige, K.; Yamada, H. *Rev. Sci. Instrum.* **2005**, *76*, 053704. doi:10.1063/1.1896938
- Colchero, J.; Cuenca, M.; Martínez, J. F. G.; Abad, J.; García, B. P.; Palacios-Lidón, E.; Abellán, J. *J. Appl. Phys.* **2011**, *109*, 024310. doi:10.1063/1.3533769
- Ekinci, K. L.; Yang, Y. T.; Roukes, M. L. *J. Appl. Phys.* **2004**, *95*, 2682. doi:10.1063/1.1642738
- Gauthier, S. J. *Appl. Phys.* **2011**, *110*, 036107. doi:10.1063/1.3619776
- Colchero, J.; Francisco González Martínez, J.; Abad, J.; Pérez García, B.; Cuenca, M.; Palacios-Lidón, E.; Abellán, J. *J. Appl. Phys.* **2011**, *110*, 036108. doi:10.1063/1.3619795
- Giessibl, F. J.; Hembacher, S.; Bielefeldt, H.; Mannhart, J. *Science* **2000**, *289*, 422–425. doi:10.1126/science.289.5478.422
- Giessibl, F. J.; Hembacher, S.; Herz, M.; Schiller, C.; Mannhart, J. *Nanotechnology* **2004**, *15*, S79–S86. doi:10.1088/0957-4484/15/2/017
- Giessibl, F. J. *Science* **1995**, *267*, 68–71. doi:10.1126/science.267.5194.68

50. Uchihashi, T.; Sugawara, Y.; Tsukamoto, T.; Ohta, M.; Morita, S.; Suzuki, M. *Phys. Rev. B* **1997**, *56*, 9834–9840.
doi:10.1103/PhysRevB.56.9834
51. Erlandsson, R.; Olsson, L.; Mårtensson, P. *Phys. Rev. B* **1996**, *54*, R8309–R8312. doi:10.1103/PhysRevB.54.R8309
52. Kawai, S.; Kawakatsu, H. *Appl. Phys. Lett.* **2006**, *88*, 133103.
doi:10.1063/1.2189193
53. Jaafar, M.; Martínez-Martín, D.; Cuenca, M.; Melcher, J.; Raman, A.; Gómez-Herrero, J. *Beilstein J. Nanotechnol.* **2012**, *3*, 336–344.
doi:10.3762/bjnano.3.38
54. Giessibl, F. J. *Rev. Mod. Phys.* **2003**, *75*, 949–983.
doi:10.1103/RevModPhys.75.949
55. Jarvis, S. P.; Yamada, H.; Kobayashi, K.; Toda, A.; Tokumoto, H. *Appl. Surf. Sci.* **2000**, *157*, 314–319.
doi:10.1016/S0169-4332(99)00545-0
56. Horcas, I.; Fernández, R.; Gómez-Rodríguez, J. M.; Colchero, J.; Gómez-Herrero, J.; Baro, A. M. *Rev. Sci. Instrum.* **2007**, *78*, 013705.
doi:10.1063/1.2432410

License and Terms

This is an Open Access article under the terms of the Creative Commons Attribution License (<http://creativecommons.org/licenses/by/2.0>), which permits unrestricted use, distribution, and reproduction in any medium, provided the original work is properly cited.

The license is subject to the *Beilstein Journal of Nanotechnology* terms and conditions: (<http://www.beilstein-journals.org/bjnano>)

The definitive version of this article is the electronic one which can be found at:
[doi:10.3762/bjnano.4.15](https://doi.org/10.3762/bjnano.4.15)